

3D MERMAID: 3D Multi-shot enhanced recovery motion artifact insensitive diffusion for submillimeter, multi-shell, and SNR-efficient diffusion imaging

Sajjad Feizollah^{1,2}  | Christine L. Tardif^{1,2,3} 

¹Department of Neurology and Neurosurgery, Faculty of Medicine and Health Sciences, McGill University, Montreal, Quebec, Canada

²McConnell Brain Imaging Centre, Montreal Neurological Institute, McGill University, Montreal, Quebec, Canada

³Department of Biomedical Engineering, Faculty of Medicine and Health Sciences, McGill University, Montreal, Quebec, Canada

Correspondence

Christine L. Tardif, Department of Neurology and Neurosurgery, Faculty of Medicine and Health Sciences, McGill University, Montreal, QC, Canada.
Email: christine.tardif@mcgill.ca

Funding information

Canadian Foundation for Innovation; Natural Sciences and Engineering Research Council of Canada, Grant/Award Number: NSERC-RGPIN-2018-05176; Fonds de recherche du Québec - Nature et technologies; Fonds de Recherche du Québec - Santé, Grant/Award Number: FRQS-CB-350681; Healthy Brains Healthy Lives; Fondation Brain Canada

Abstract

Purpose: To enhance SNR per unit time of diffusion MRI to enable high spatial resolution and extensive q-sampling in a feasible scan time on clinical scanners.

Methods: 3D multi-shot enhanced recovery motion-insensitive diffusion (MERMAID) consists of a whole brain nonselective 3D multi-shot spin-echo sequence with an inversion pulse immediately before the excitation pulse to enhance the recovery of longitudinal magnetization. The excitation flip angle is reduced to the Ernst angle. The sequence includes a trajectory using radially batched internal navigator echoes (TURBINE) readout, where a 3D projection of the FOV is acquired at a different radial angle in every shot. An image-based phase-correction method combined with compressed sensing image reconstruction was developed to correct phase errors between shots. The performance of the 3D MERMAID sequence was investigated using Bloch simulations as well as phantom and human scans at 3 T and then compared to a typical multi-slice 2D spin-echo sequence.

Results: Improvements in SNR per unit time of 70%–240% were observed in phantom and human scans when using 3D MERMAID compared to a single-slice 2D spin-echo sequence. This SNR per unit time improvement allowed scans to be acquired at a nominal isotropic resolution of 0.74 mm and a total of 112 directions across four shells ($b = 150, 300, 1000, 2000 \text{ s/mm}^2$) in 37 min on a clinical scanner.

Conclusion: The 3D MERMAID sequence was shown to significantly improve SNR per unit time compared to multi-slice 2D and 3D diffusion sequences. This SNR improvement allows for shorter scan times and higher spatial and angular resolutions on clinical scanners.

KEYWORDS

3D diffusion MRI, high spatial resolution, phase correction, SNR per unit time, TURBINE

1 | INTRODUCTION

High-resolution diffusion MRI (dMRI) is a powerful tool to map the microstructure of small structures across the entire brain. Ex vivo dMRI studies of healthy human brains have been performed at isotropic resolutions of $\sim 100\text{--}650\text{ }\mu\text{m}$ and validated using histology.^{1–4} These studies have revealed the complex geometry and microstructure of crossing fibers in the white matter (WM), the layered intracortical myeloarchitecture showing radial and tangential cortical projections as well as short-range U-fibers.^{5–7} High-resolution postmortem dMRI has also revealed microstructural alterations of cortical gray matter (GM) and small structures in patients such as the hippocampus in Alzheimer's,⁸ seizures,⁹ and hippocampal sclerosis¹⁰; the substantia nigra in Parkinson's¹¹; and the corpus callosum in amyotrophic lateral sclerosis.¹² In contrast, the in vivo spatial resolution is limited due to the inherently low SNR of dMRI, resulting in nominal resolutions of $\sim 2.5\text{--}1.5\text{ mm}$ for scans performed in a reasonable scan time for most clinical and research scans. These high-resolution ex vivo and in vivo dMRI studies have motivated the development of MRI techniques to enhance SNR efficiency of in vivo dMRI to achieve high-resolution imaging in clinical scan times.

Conventional dMRI employs a 2D single-shot acquisition of a spin-echo (SE) sequence with an EPI readout. Using this sequence, whole brain spatial resolutions of $2.5\text{--}1.5\text{ mm}$ are achievable at 3 T, benefiting from techniques such as partial Fourier^{13,14} and parallel imaging^{15–17} to shorten the EPI train. Furthermore, simultaneous multi-slice imaging^{18,19} significantly shortens the TR, allowing for the acquisition of more volumes with different diffusion encodings (e.g., directions, b -values, diffusion times) within a reasonable scan time. Whereas these methods are used to reconstruct WM tracts and obtain valuable microstructural details through multi-compartment tissue models,^{20–22} the tissue within the achievable voxel size is highly complex due to partial volume effects with different fiber populations, GM structures, and CSF, highlighting the need for further improvement in resolution.

Pushing the resolution using these conventional methods requires lengthening the readout, which results in longer TEs, excessive artifacts and distortions, and lower SNR due to T_2 decay. New image acquisition approaches have been proposed to mitigate these problems and increase SNR. Most techniques for high-resolution dMRI have relied on multi-shot SE acquisitions at the cost of scan time. They often require the integrated acquisition of a navigator to correct phase errors between shots caused by microscopic and macroscopic motion.²³ The navigator can be acquired by adding a refocusing pulse at the end of the image readout.^{24–26} Alternatively, a self-navigating

readout trajectory such as variable density spirals and key-hole trajectories can be used.^{27,28} Recent multi-shot acquisition techniques use navigator-free approaches such as multiplexed sensitivity encoding (MUSE) and multishot sensitivity-encoded recovery using structured low-rank matrix (MUSSELS) completion^{29–31} that take advantage of the smoothness of the phase of each shot. Low-rank Hankel matrix techniques have also been used to solve for a smoothly varying phase, assuming the magnitude of each shot is consistent.³² Other multi-shot acquisition approaches based on the periodically rotated overlapping parallel lines with enhanced reconstruction (PROPELLER) readout^{33–35} eliminate the need for an additional navigator scan. This fast spin-echo sequence provides a robust artifact-free solution suitable for clinical settings in which the specific absorption rate (SAR) and low number of diffusion directions are not limiting. Super-resolution techniques are another category of multi-shot imaging techniques that reconstruct high-resolution images from a series of lower resolution scans with translation or rotation.^{36,37} Most recently, rotating-view motion-robust super resolution (ROMER) is combined with echo planar time-resolved imaging (EPTI) to achieve images at 3 T with an isotropic resolution of $500\text{ }\mu\text{m}$, b -value of 1000 s/mm^2 , and 25 diffusion directions in 80 min.³⁸ In addition to the multi-shot 2D dMRI techniques described above, 3D multi-slab approaches in which a slab of brain is excited and acquired in multiple shots have been proposed to enhance resolution.^{39,40} The same 2D navigator-based methods are applied with the assumption that phase changes in the slice direction are small for slabs $\leq 2\text{ mm}$.^{40,41} Alternatively, multiple RF pulse profiles can be used to differently encode slice information in a thick slab acquired in multiple shots as in g-Slider.^{42–45}

There are few 3D acquisition techniques for dMRI that use a whole brain excitation. As for anatomical imaging, these 3D techniques employ steady-state sequences with a short TR.^{46,47} A 3D SSFP sequence was proposed by McNab et al. for high SNR in vivo and ex vivo imaging using the trajectory using radially batched internal navigator echoes (TURBINE) readout.⁴⁸ The main disadvantages of this technique are the complex T_2/T_1 and diffusion contrast, and high sensitivity to motion that limits its application in vivo. A 3D gradient and spin echo sequence that uses a 3D navigator to correct for phase errors was also recently proposed.⁴⁹ Instead of estimating and correcting for phase errors between shots, some 3D dMRI sequence implementations use motion-compensated diffusion-encoding gradients to minimize phase errors.^{50,51} This type of diffusion encoding requires longer encoding times that result in longer TEs and lower SNR. The TEs can be shortened by using high-performance gradient systems when available.⁵²

Most of the multi-shot 2D and 3D dMRI techniques reviewed above increase SNR efficiency and achieve high-resolution images, but they also have long scan times. Whereas these techniques and protocols differ in terms of SNR efficiency and image quality, the effective TRs range from ~ 45 s at 0.76 mm, with a maximum b -value of 2500 s/mm²,⁴⁵ to ~ 3.2 min at 0.5 mm with a maximum b -value of 1000 s/mm².³⁸ These long scan times limit the number of diffusion encodings that can be acquired within a scanning session. Microstructure models, in particular of the GM, require extensive q -space sampling and/or multi-echo and multi-diffusion time experiments.^{53–55} Therefore, although the anatomical specificity is enhanced using the high-resolution techniques described above, the microstructural interpretation of the data remains limited. More efficient sequences are needed to fully utilize the potential of high-resolution dMRI for in vivo applications.

We developed a whole brain 3D multi-shot enhanced recovery motion insensitive diffusion-weighted (MERMAID) sequence that improves SNR per unit time compared to a 2D SE sequence and keeps the scan time per volume short.⁵⁶ Going from 2D to 3D for high-resolution imaging improves SNR, spin history, and B_1^+ uniformity and also eliminates slab/slice profile artifacts. However, several challenges need to be addressed. First, the available steady state signal is low due to saturation of the longitudinal magnetization caused by the short TR in a SE sequence. This was addressed by adding an inversion pulse before the excitation and reducing the excitation flip angle. The second challenge is phase errors between shots caused by macroscopic motion and cardiac cycles. A TURBINE readout with a new image reconstruction pipeline was developed to correct for these errors. We demonstrate that this SNR-efficient 3D dMRI technique can be used to acquire high spatial resolution images, up to 0.74 mm isotropic with maximum b -value of 2000 s/mm² in 112 directions in 37 min (corresponding to 19 s per volume), suitable for high-resolution microstructural mapping.

2 | METHODS

2.1 | 3D steady-state SE dMRI with enhanced longitudinal magnetization recovery

The simplest way of creating a 3D diffusion sequence is to change the excitation and refocusing pulses into 3D pulses, minimize TR, and add phase encoding along the slice direction to create a multi-shot 3D readout trajectory (henceforth referred to as the 3D SE sequence). Instead of lengthening the TR to improve signal recovery, we propose

a novel sequence referred to as 3D MERMAID, illustrated in Figure 1A. This sequence significantly enhances signal recovery in the 3D SE sequence by incorporating an inversion pulse immediately before excitation. To demonstrate the mechanism, we performed Bloch simulations comparing 3D MERMAID with a 3D SE sequence. These simulations used a TE of 64 ms and T_1/T_2 of 866/71 ms, consistent with the T_1 of WM at 3 T.^{57,58} Figure 1B shows that in a traditional dMRI sequence with 90- and 180-degree pulses, reducing the TR leads to prolonged recovery times for the longitudinal magnetization transitioning from negative to positive, resulting in a reduced steady-state signal. By inserting an inversion pulse just before the excitation, as depicted in Figure 1C, the longitudinal magnetization is flipped back to the positive side by the refocusing pulse, thereby enhancing signal recovery until the next TR.

According to the Bloch equations⁵⁹ and the sequence diagram in Figure 1A, the steady-state longitudinal magnetization $M_{z_{ss}}$ is described by Equation (1):

$$M_{z_{ss}} = \frac{e^{\frac{TI}{T_1}} (\cos(\alpha) - 1) - e^{\frac{TR}{T_1}} + 2e^{\frac{TE}{2} + \frac{TI}{T_1}} - \cos(\alpha)}{-e^{\frac{TR}{T_1}} + \cos(\alpha)}. \quad (1)$$

Here, TI represents the time between the inversion and excitation pulses, and α is the excitation flip angle. The transverse magnetization at the TE $M_{xy_{TE}}$ is calculated by Equation (2).

$$M_{xy_{TE}} = \frac{e^{\frac{TI}{T_1}} (\cos(\alpha) - 1) - e^{\frac{TR}{T_1}} + e^{\frac{TE}{2} + \frac{TI}{T_1}} - \cos(\alpha)}{-e^{\frac{TR}{T_1}} + \cos(\alpha)} \cdot \sin(\alpha) \cdot e^{-\frac{TE}{T_2}}. \quad (2)$$

To maximize the $M_{xy_{TE}}$, an optimal excitation flip angle must be employed. Determining this flip angle using Equations (1) and (2) yields the Ernst angle formula for gradient echo sequences,⁶⁰ shown in Equation (3).

$$\alpha_{\text{Ernst}} = \arccos \left(e^{\left(-\frac{TR}{T_1} \right)} \right). \quad (3)$$

2.2 | Image reconstruction and motion correction

Another challenge of multi-shot 3D SE imaging is sensitivity to intershot phase errors. We implemented the TURBINE^{48,61} strategy, as shown in Figure 1D. Each shot acquires a radial plane of k -space rotated around the anteroposterior axis such that each is individually reconstructed into a projection of the FOV. The acquisition is accelerated by undersampling each EPI plane, similar to a 2D EPI readout ($R_{\text{in-plane}}$), and undersampling in the projection dimension ($R_{\text{projection}}$), which requires $N\pi/2$

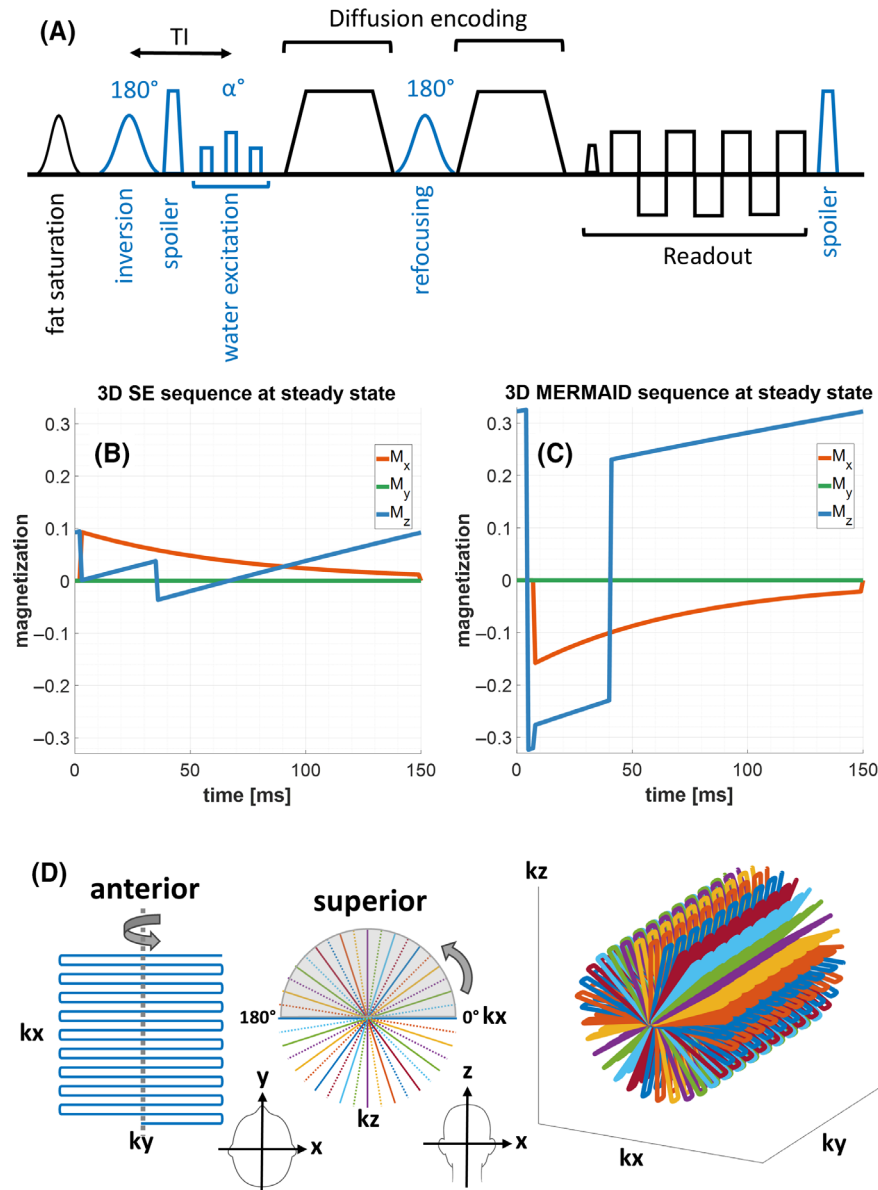


FIGURE 1 Sequence diagram, Bloch simulations, and the readout of the 3D MERMAID sequence. (A) Sequence diagram shows the new components added to a conventional SE sequence in blue: an inversion pulse, spoilers, and nonselective pulses. (B) Shows one TR of a 3D SE sequence at the steady state. (C) Shows Bloch simulation of the 3D MERMAID sequence at the steady state. (D) TURBINE readout (undersampled due to better visualization) constructed from a 2D EPI plane rotating around anteroposterior axis. Each color shows a shot, and projections specified by dotted line are skipped to accelerate the scan in the radial direction. MERMAID, multi-shot enhanced recovery motion insensitive diffusion; TURBINE, trajectory using radially batched internal navigator echoes.

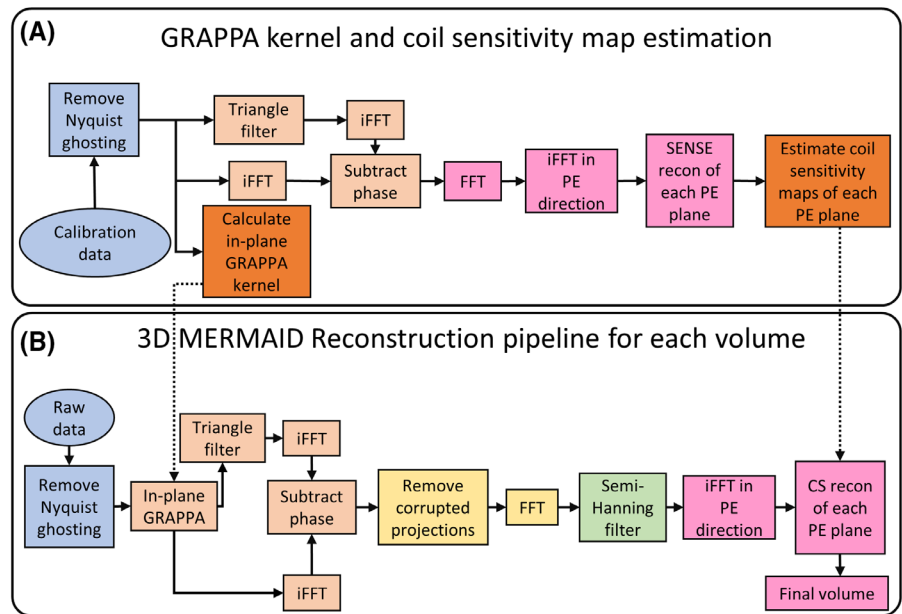
projections to meet the Nyquist criteria where N is the matrix size. Partial Fourier is also applied within each radial plane in the EPI phase-encode direction as typically employed in 2D EPI readouts.

The 3D dMRI TURBINE image reconstruction pipeline is summarized in Figure 2. A generalized autocalibrating partially parallel acquisitions (GRAPPA) kernel¹⁵ is estimated for in-plane (k_x - k_y) projection reconstruction, and coil sensitivity maps are estimated for a compressed sensing (CS) reconstruction¹⁷ of each phase-encode (PE) plane (k_x - k_z) with radial sampling as depicted in Figure 2A. The raw k-space data from the calibration scans are corrected for Nyquist ghosting using the method described by Heid.⁶² From the corrected data, the in-plane GRAPPA kernel for each projection is estimated as for a typical 2D GRAPPA reconstruction. Before estimating coil sensitivity maps for each PE plane,⁶³ the phase of each projection is

removed using a triangle filter with a width of 0.25, as suggested in Ref. 64, similar to the method used by Pipe et al.⁶⁵ and Wang et al.⁶⁶ for removing motion-corrupted phase.

Once the GRAPPA kernel and coil sensitivity maps are calculated, scans are reconstructed using the pipeline shown in Figure 2B. Nyquist ghost correction and phase correction are done as previously described. Motion related to the cardiac cycle also corrupts the k-space data and introduces significant deviations in image magnitude. These artifacts appear as large hypointense areas in regions of significant motion such as the ventricles and spine. To identify the corrupted projections, we compare the total image signal of each projection against the average across all projections. The projections that deviate significantly from the average are removed. This method eliminates the need to record cardiac rhythm or make the acquisition cardiac gated. The motion-corrected

FIGURE 2 Image reconstruction pipeline. (A) Method used to calculate in-plane GRAPPA kernels and coil sensitivity of each PE plane. (B) Pipeline used to reconstruct each volume with motion correction. FFT, fast Fourier transform; iFFT, inverse fast Fourier transform; PE, phase-encode.



k-space data are subsequently obtained by computing the inverse Fourier transformation of the corrected projections. To eliminate Gibbs ringing artifacts along the frequency-encode (FE) direction, a semi-Hanning filter is applied to the outer 20% of k-space representing high-frequency components in the FE direction. Lastly, projections are combined using an inverse fast Fourier transformation along the PE direction, followed by CS reconstruction of each PE plane using the Berkeley Advanced Reconstruction (BART) toolbox.^{67,68} Output of each step of the reconstruction pipeline is shown in Figure S1.

The reconstructed images can be postprocessed using the tools developed for 2D EPI scans. Due to the long readout duration of each shot of the TURBINE trajectory, B_0 field inhomogeneities cause artifacts in the images that appear similar to EPI distortion artifacts. An image with an opposite PE direction is acquired and used to correct these artifacts⁶⁹ with *topup* and *eddy* implemented in FMRIB Software Library.⁷⁰ To achieve optimal denoising results, the image reconstruction pipeline was modified to include a denoising step right after the reconstruction of projections, as shown in Figure S2.

2.3 | Bloch simulations to optimize the 3D MERMAID sequence

The SNR per unit time of the 3D MERMAID sequence is affected by various factors, including TR, flip angle, and B_1^+ uniformity. To explore the impact of these parameters on the sequence's efficiency, four Bloch simulations were conducted.

The first simulation aimed to compare the signal recovery enhancement using the 3D MERMAID sequence

versus the 3D SE sequence across various b -values and resolutions. This simulation was performed with TEs and TRs adjusted to b -values of 1000, 2000, and 3000 s/mm², and a T_1 of 866 ms, alongside readouts matching the nominal resolution range of 0.8 to 1.5 mm achievable by the standard Siemens diffusion sequence. The excitation flip angle was adjusted to the Ernst angle for the corresponding TR. The analysis focused on the steady-state transverse magnetization of the 3D MERMAID sequence and the conventional 3D SE sequence, highlighting the signal recovery improvements.

The steady-state signal is sensitive to the flip angle of the inversion and refocusing pulses. A second Bloch simulation was performed to assess the impact of B_1^+ field variations, ranging from 0.4 to 1.4 times the nominal value, on the 3D SE and 3D MERMAID signals, and a T_1 of 866 ms.

A third Bloch simulation was performed to study the effect of TR on the steady-state transverse magnetization at the TE. This was done for the WM, GM, and CSF with T_1/T_2 relaxation times of 866/71 ms, 1300/72 ms, and 4160/1700 ms, respectively,^{57,58} for a range of TRs from 100 to 300 ms.

Lastly, the effect of varying flip angle between 1 and 90 degrees on the steady-state transverse magnetization at TE was simulated with the same relaxation times above and a TR of 150 ms.

2.4 | Phantom scans to compare relative SNR of 3D MERMAID with 2D SE sequence

All scans were performed on a 3 T Prisma-Fit Siemens scanner running VE11C software (Siemens, Erlangen,

Germany). The 3D MERMAID sequence was developed by modifying the Siemens diffusion sequence (henceforth referred to as the 2D SE sequence). An amplitude-modulated hyperbolic secant adiabatic pulse of 5120 μs was implemented for inversion and refocusing. To ensure complete fat signal suppression, a fat saturation pulse was applied before the inversion pulse, and a non-selective water excitation pulse was implemented, as illustrated in Figure 1A. To prevent stimulated echoes, gradient spoiling was applied immediately following the inversion pulse and the readout, and RF spoiling was applied to the inversion and excitation pulses.

For the readout, a TURBINE trajectory was implemented as in Figure 1D, in which each shot is a rotated version of the single-shot 2D EPI trajectory around the anteroposterior axis, chosen for minimum peripheral nerve stimulation.

To compare the SNR of the 3D MERMAID sequence with that of the 2D SE sequence, we prepared a spherical phantom with T_1 relaxation times of ~ 868 ms to model the WM. To compute the SNR, 15 repetitions at nominal resolutions of 0.86, 1.0, 1.2, and 1.5 mm were acquired using the scan parameters specified in Table 1. Additionally, scans across a range of TEs and TRs corresponding to b -values of 0, 1000, 2000, and 3000 s/mm^2 were performed without employing diffusion-encoding gradients to avoid a signal loss due to the high diffusivity of the phantom. The 3D MERMAID scans were retrospectively undersampled in the projection dimensions ($R_{\text{projection}} = 1, 2, 3, 4$) to investigate the impact of undersampling on the relative SNR. One hundred twenty-eight slices were acquired using 2D SE for all resolutions due to a limitation in the VE11C version of the Siemens diffusion sequence. The 3D MERMAID scans were reconstructed using SENSE instead of CS, and no further postprocessing was employed for 2D SE or 3D MERMAID. The SNR was assessed in the center of the spherical phantom within a FOV of $100 \times 100 \times 100$ mm by dividing the magnitude of the first scan by the SD of the noise, derived from the 15 repetitions.

2.5 | Removal of motion artifacts in reconstruction of 3D images

All human scans received approval from the Research Ethics Board of the Montreal Neurological Institute, and informed consent was obtained from all participants.

The following scans were performed to test the motion correction strategy and compare the resulting diffusion metrics in brain tissue with the standard Siemens 2D SE

sequence. A participant (male, 25 years old) was scanned using both the 2D SE and 3D MERMAID sequences at an isotropic nominal resolution of 1.2 mm, b -values of 1000 and 2000 s/mm^2 with 12 diffusion directions each. Remaining acquisition parameters are detailed in Table 1. For the 3D MERMAID sequence, all projections were acquired to meet the Nyquist criteria and retrospectively undersampled by a factor of 3 to match the scan time of the 2D SE sequence. The subject's pulse was recorded and subsequently used to study the effects of the cardiac cycle on the diffusion images.

Scans acquired with the 2D SE sequence were processed using *mrdegibbs* to minimize Gibbs ringing artifacts. The fractional anisotropy (FA), direction-encoded color (DEC), and ADC maps were generated using MRtrix3.^{71–73}

2.6 | 2D SE and 3D MERMAID comparison at submillimeter resolution

To demonstrate the performance of the 3D MERMAID compared to the 2D SE sequence in acquiring high spatial and angular resolution scans, a second participant (female, 27 years old) was scanned. A multi-shell protocol was used for microstructural modeling with matching acquisition parameters: a nominal isotropic resolution of 0.9 mm and b -values of 0, 150, 300, 1000, and 2000 s/mm^2 in 1, 7, 10, 30, 64 directions, respectively, totaling 112 directions. The $b = 0$ s/mm^2 image was only used for motion correction using *eddy*. To reduce the impact of pulsatile CSF signal close to the cerebellum, which causes strong streaking artifacts in the 3D MERMAID, a low b -value of 150 s/mm^2 was used for subsequent estimation of diffusion metrics. To calculate SNR maps, 20 averages of a b -value of 150 s/mm^2 were acquired using both sequences. Other scan parameters are listed in Table 1. A T_1 -weighted CS MPRAGE sequence⁷⁴ with a nominal resolution of 1 mm was acquired for anatomical reference. The 2D SE scans were reconstructed using the scanner's image reconstruction pipeline, which included projection onto convex sets (POCS) to recover resolution due to partial Fourier. Magnitude and phase images were used for denoising by applying noise reduction with the distribution-corrected (NORDIC) method.⁷⁵ The 3D MERMAID scans were reconstructed using the image reconstruction pipeline in Figure S2, including projection onto convex sets and NORDIC. The 2D SE and 3D MERMAID scans used for calculating the SNR maps were not denoised by applying the NORDIC method.

Reconstructed scans from both dMRI sequences were postprocessed and analyzed as described in section 2.5.

TABLE 1 Parameters of phantom and human scans.

Phantom scans										
Scan			2D EPI				3D MERMAID			
b-value			0	1000	2000	3000	0	1000	2000	3000
TE/TR (ms)	Isotropic resolution (mm)	0.86	79/ 19500	86/ 20400	92/ 21200	97/ 23300	78/ 160	85/ 166	91/ 172	96/ 188
		1.0	65/ 16000	74/ 17100	80/ 20400	85/ 23400	64/ 144	73/ 144	79/ 164	84/ 187
		1.2	52/ 12500	62/ 16200	69/ 20700	75/ 23300	51/ 144	61/ 144	68/ 167	73/ 192
		1.5	45/ 10700	56/ 15000	63/ 19800	69/ 22600	44/ 144	56/ 144	63/ 160	69/ 181
FOV (mm)			240×240							
Number of slices/ projections	Isotropic resolution (mm)	0.86	128				402			
		1.0					345			
		1.2					314			
		1.5					232			
R _{in-plane}			3							
R _{slice} /R _{projection}			1/1							
PF factor			6/8							
Echo spacing (ms)	Isotropic resolution (mm)	0.86	1.32							
		1.0	1.16							
		1.2	0.97							
		1.5	0.93							
In-vivo scans										
Scan	Initial		Comparing 2D and 3D				High-resolution			
	2D SE	3D MERMAID	Multi-shell protocol		SNR calculation		3D MERMAID			
			2D SE	3D MERMAID	2D SE	3D MERMAID				
Nominal isotropic resolution (mm)	1.2		0.9		0.9	0.9	0.74			
FOV (mm)	240×240		198×198		198×198		198×198			
Total number of slices*/projections	126	314	126	345	126	345	420			
R _{in-plane}	2	2	3		3		3			
R _{slice} /R _{projection}	2	1	2	4	2	4	6			
PF factor	5/8		5/8		5/8		5/8			
TE/TR (ms)	71/10700	69/174	70/9700	68/170	70/9700	68/170	74/280			
b-value (s/mm²)	0, 1000, 2000		0, 150, 300, 1000, 2000		150		0, 150, 300, 1000, 2000			
Number of diffusion directions (total)	2, 12, 12 (26)		1, 7, 10, 30, 64 (112)		20 (same direction)		1, 7, 10, 30, 64 (112)			
Echo spacing (ms)	0.98		1.26		1.26		1.26			
Scan time (min)**	8	24	26	26	6	6	37			

Note: Phantom and human scans acquired to compare the 3D MERMAID and 2D SE sequences and to optimize 3D MERMAID sequence.

MERMAID, multi-shot enhanced recovery motion insensitive diffusion. PF, partial Fourier.

*Maximum available number of slices in the standard Siemens diffusion sequence in VE11C.

**Total scan time for 2D SE was adjusted for a FOV of 160 mm in the slice direction.

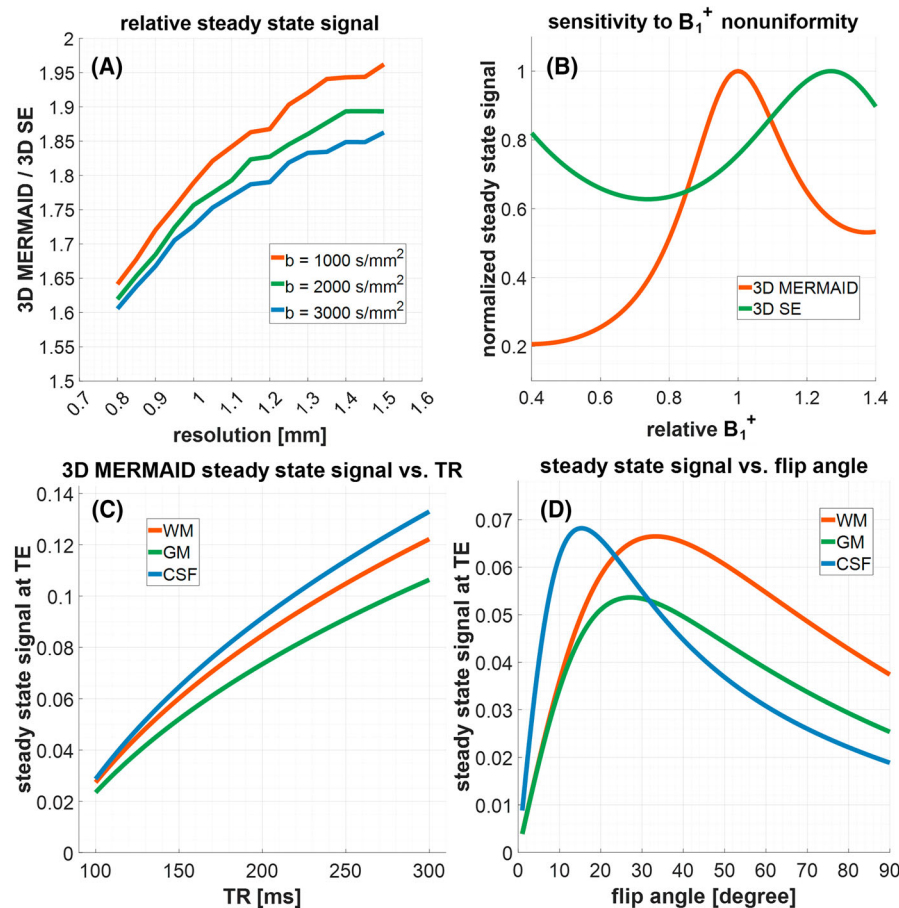


FIGURE 3 Bloch simulations to determine the performance of the 3D MERMAID sequence. (A) Ratio of the available transverse magnetization of the 3D MERMAID sequence and a 3D SE sequence at different TEs/TRs corresponding to b-values of 1000, 2000, and 3000 s/mm². (B) Sensitivity of the 3D MERMAID sequence to B_1^+ nonuniformity compared to a 3D SE sequence. (C) The transverse magnetization at steady state as a function of TR for three tissues. (D) Changes in transverse magnetization of GM, WM, and CSF with flip angle. CSF, Cerebrospinal fluid; GM, gray matter; SE, spin echo; WM, white matter.

Additionally, fiber orientation distribution functions (fODFs) were estimated using all shells in MRTrix3.^{71,76–80} The MPRAGE scan was then nonlinearly registered to each diffusion sequence separately using advanced normalization tools (ANTs).^{81,82} GM and WM were then segmented using FMRIB Software Library's *fast* function.^{70,83}

2.7 | Pushing the spatial resolution of 3D MERMAID

To demonstrate the capability of the 3D MERMAID sequence in acquiring high spatial and angular resolution scans within a reasonable scan time, a third participant (male, 24 years old) was scanned using the same multi-shell diffusion-encoding protocol (112 volumes in total) as the previous scan, with a nominal isotropic resolution of 0.74 mm. The TR was set to 280 ms to improve the SNR, resulting in a total scan time of 37 min. Other scan parameters are listed in Table 1. The same image reconstruction, postprocessing, and analysis were performed as in the previous scan.

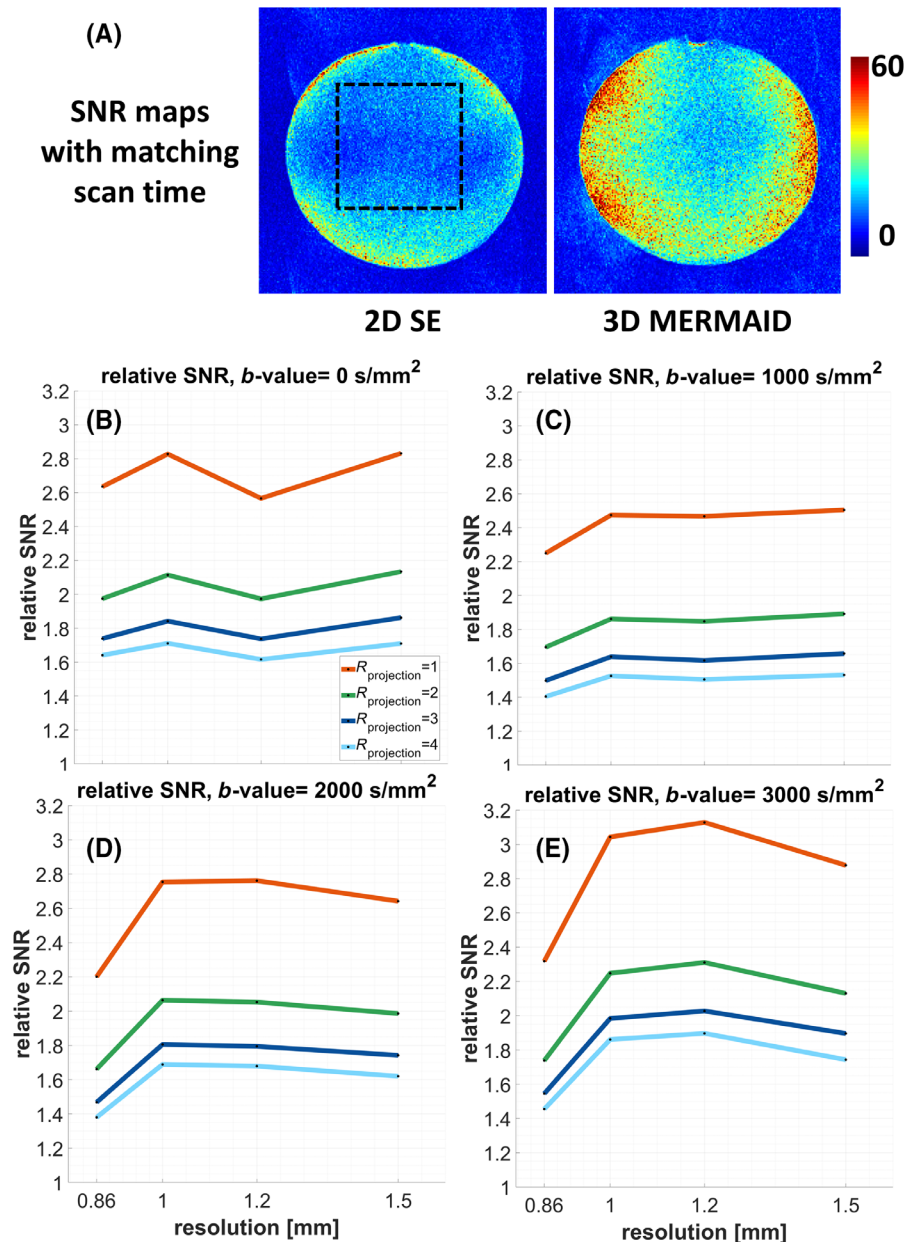
3 | RESULTS

3.1 | Bloch simulations to evaluate the performance of the 3D MERMAID sequence

Figure 3A illustrates the ratio between the steady-state transverse magnetization of the 3D MERMAID sequence and the 3D SE sequence. By employing the Ernst angle for excitation, the 3D MERMAID sequence enhances signal recovery by ~64% and ~96% at resolutions of 0.8 and 1.5 mm, respectively. However, while TE and TR increase at higher b-values, this enhancement in signal recovery diminishes slightly.

The sensitivity of the 3D MERMAID sequence to B_1^+ nonuniformity is shown in Figure 3B. When the relative B_1^+ field varies from 0.4 to 1.4, the transverse magnetization at steady state experiences a nonlinear change of approximately 80% in the 3D MERMAID, compared to about 38% in the 3D SE sequence. These results underscore the importance of achieving uniform RF pulse profiles across the volume to maintain the signal recovery enhancement of the 3D MERMAID sequence in all regions.

FIGURE 4 SNR map and relative SNR of the 3D MERMAID sequence compared to 2D SE sequence at different TEs/TRs. (A) SNR maps of a 2D SE and 3D MERMAID sequence at nominal isotropic resolution of 1 mm. The scan times for both scans are matched to show the SNR per unit time of the 3D MERMAID sequence. The area at the center of the phantom used to calculate the relative SNR is specified as dotted line. (B–E) SNR of the 3D MERMAID sequence relative to the 2D SE sequence at the center of the phantom for different timings corresponding to b -values of 0, 1000, 2000, and 3000 s/mm^2 , respectively.



The transverse magnetization at TE for three tissues (WM, GM, and CSF) as a function of TR is plotted in Figure 3C. When the TR is increased from 100 to 300 ms, the available signal rises from ~ 0.02 for all tissues, to ~ 0.1 , ~ 0.12 , and ~ 0.13 for GM, WM, and CSF, respectively. This represents a \sim six-fold increase in the available signal when the TR is tripled.

Figure 3D illustrates changes in the steady-state transverse magnetization as a function of the excitation flip angle. It shows a nonlinear change in the available signal at TE, with a maximum occurring at the Ernst angle for each tissue as described above.

3.2 | Phantom scans show improved SNR for 3D MERMAID compared to 2D SE sequence

Figure 4A showcases the higher SNR of the 3D MERMAID sequence in comparison to the conventional 2D SE sequence in the phantom at 1 mm resolution. Both sequences have approximately the same scan time per volume of 12 s and use the same in-plane acceleration factor of 3. Although there was no slice acceleration applied in 2D SE sequence, an acceleration factor of 2 is required to achieve this scan time, which does not affect the SNR

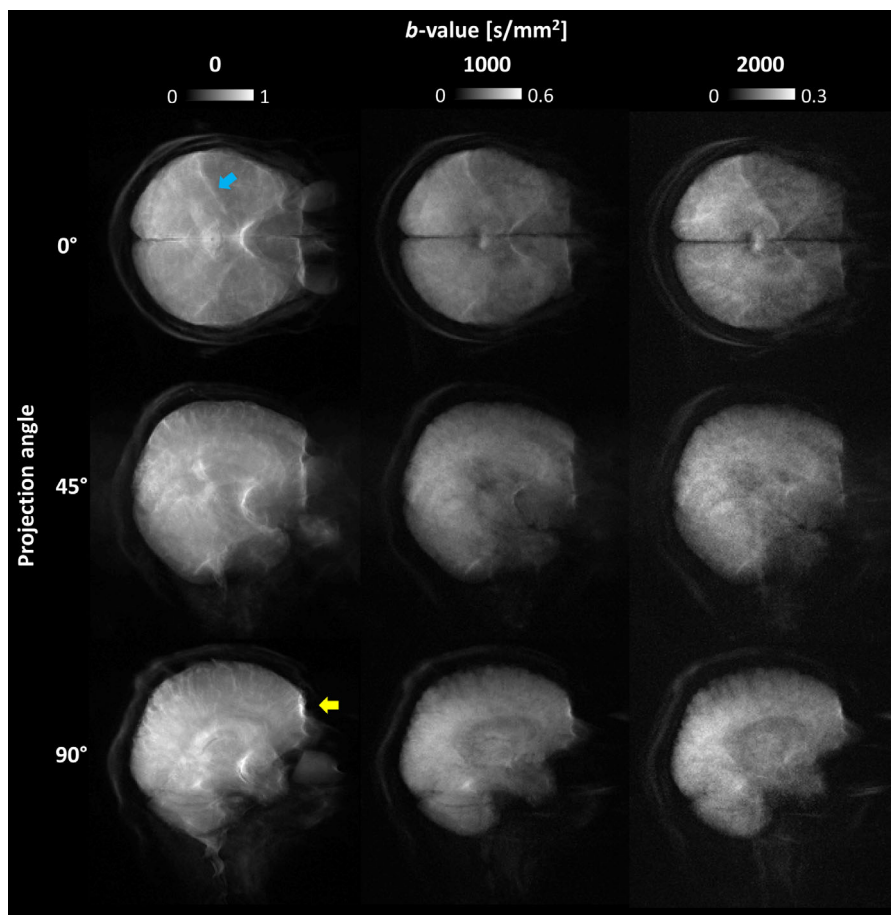


FIGURE 5 Raw projections acquired at b -values of 0, 1000, and 2000 s/mm^2 in 0, 45, and 90° angles. Each projection is independently reconstructed showing the brain overlaying on a single image. Blue and yellow arrows show artifacts due to ΔB_0 nonuniformities.

significantly. The 3D MERMAID sequence employs a projection acceleration factor of 4 to reduce the scan time per volume.

The SNR of the 3D MERMAID sequence relative to the 2D SE sequence for the TEs and TRs associated with b -values of 0, 1000, 2000, and 3000 s/mm^2 is depicted in Figure 4B–E. The relative SNR across different resolutions ranges between ~ 1.4 and 3, depending on the acceleration factor, with a notable exception at the resolution of 0.86 mm where the relative SNR is lower (in particular, at higher b -values). This exception is attributed to the increased duration between the inversion and refocusing pulses during which magnetization decreases. At higher b -values, longer TRs contribute to improved magnetization recovery and, consequently, higher SNR. The SNR decreases approximately as a function of the square root of the projection acceleration ($\sqrt{R_{\text{projection}}}$). In contrast, the slice acceleration in the 2D SE sequence has a minimal effect on SNR for multi-band factors of 1–3 (results not shown).

3.3 | Removal of motion artifacts in reconstructed 3D images

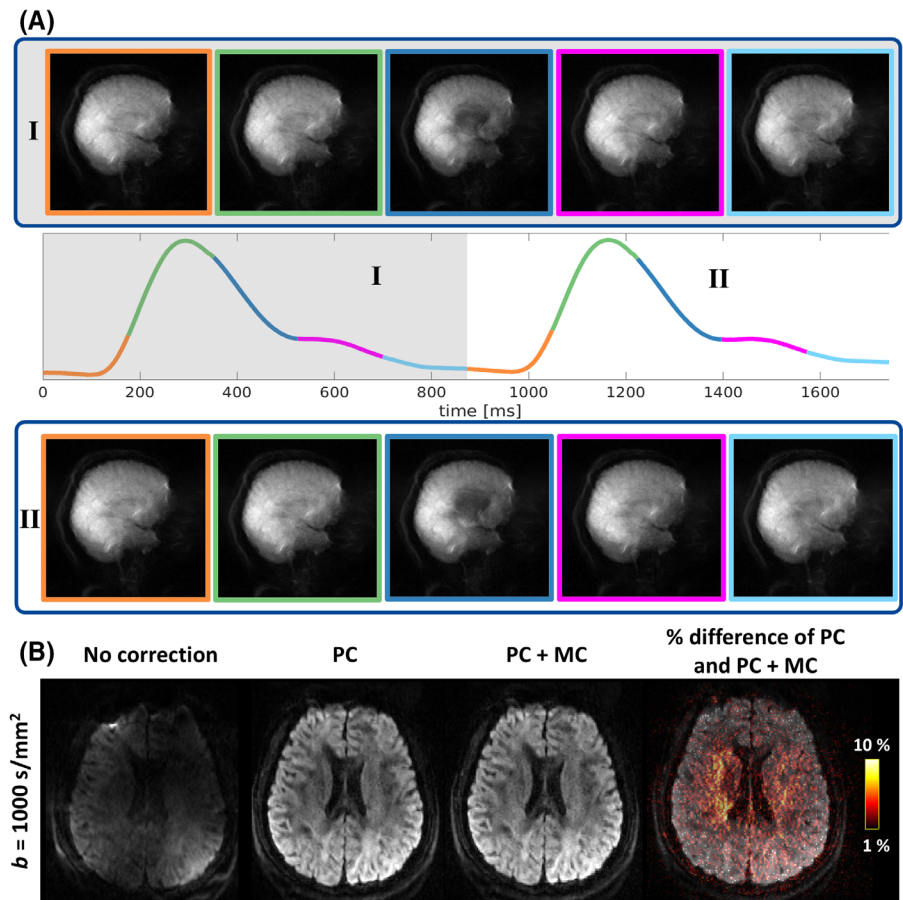
Reconstructed projections at 0, 45, and 90 degrees, acquired across different shots and b -values, are shown in

Figure 5. Each shot is independently reconstructed showing projections of the brain from different angles in a 2D image. Signal accumulation occurs in regions with high ΔB_0 , such as the frontal lobe (indicated by a yellow arrow) and around the ear canal (blue arrow), as seen in a 2D SE with an EPI trajectory. Magnitude and phase images of the reconstructed projections of each scan can be viewed in Movies S1–S3.

Figure 6A illustrates the impact of the cardiac cycle on the magnitude of the projection images acquired with a b -value of 1000 s/mm^2 . It displays 10 consecutive projections corresponding to the duration of two cardiac cycles (I and II), with colors specifying the time range at which the projections are acquired. At the third projection of both cycles, synchronized immediately after the peak of the cardiac signal, there is a visible signal drop at the center of the brain where the ventricles exhibit the greatest motion. This effect was consistently observed across all projections. For a healthy adult with a heart rate of 60–90 bpm, up to 20% of shots for the TRs used here were affected by this type of motion.

The effectiveness of the motion correction strategy on raw diffusion images is demonstrated in Figure 6B. The first column to the left presents images reconstructed without motion correction, highlighting signal drops and image artifacts. The second column shows the impact

FIGURE 6 Effects of the cardiac cycle on the magnitude images of the projections and performance of the motion correction method. (A) Shows 10 consecutive sagittal projections for two cardiac cycles. Colors of the pulse signal correspond to a phase in the cardiac cycle for which a projection is acquired. Signal drop at the center of the brain is obvious in the third projection of each cycle. (B) Performance of the motion correction when there is no correction, only PC, PC + MC, and the difference map between PC and PC + MC images overlaid to the image. MC, magnitude correction; PC, phase correction.



of removing the phase of each projection using a triangle filter (phase correction [PC]), which significantly reduces artifacts and recovers signal. The third column illustrates the results of the full motion correction method in which corrupted projections were also removed (magnitude correction [MC]), leading to further enhanced signal at the center where motion is most pronounced. The percentage difference calculated between PC and PC + MC in the last column shows up to 10% increase in signal.

The image contrast of the 3D MERMAID sequence differs from that of a typical 2D SE sequence; it has an enhanced T_1 weighting due to the shorter TR, as demonstrated in the $b = 0$ images in Figure 7A. The scans acquired using 3D MERMAID exhibit less WM–GM contrast compared to those from the 2D SE sequence.

Postprocessed images from 12 diffusion-encoding directions were used to calculate mean diffusion-weighted images, FA, and ADC maps for both sequences at two b -values of 1000 and 2000 s/mm^2 (Figure 7B). The SNR gain of the 3D MERMAID, matched for scan time with the 2D SE sequence, is clear in all diffusion maps, particularly at the center of the brain where B_1^+ nonuniformity is higher. The FA, DEC, and ADC maps are consistent across both sequences.

3.4 | 2D SE and 3D MERMAID comparison at submillimeter resolution

Figure 8 compares the 2D SE and 3D MERMAID sequences at high spatial and angular resolution. SNR maps calculated from 20 averages show an approximate 36% improvement in SNR across the entire volume with the 3D MERMAID sequence. This enhancement results in higher quality FA and ADC maps, and more significantly, less noisy fODFs derived from high b -values. Zoomed-in areas in the temporal lobe (Figure 8A,B) and anterior commissure (Figure 8C,D) clearly demonstrate improved fODFs with reduced noise contamination. The crossing fibers of the fornix and anterior commissure, shown in Figure 8E,F, are more accurately detected using the 3D MERMAID sequence. Multiple slices and views of the SNR map, mean diffusion-weighted images, DEC, ADC maps, and fODFs are presented in Figures S3–S11.

3.5 | Pushing the spatial resolution of 3D MERMAID

High-resolution diffusion maps and fODFs derived from the nominal 0.74 mm isotropic scan are presented in

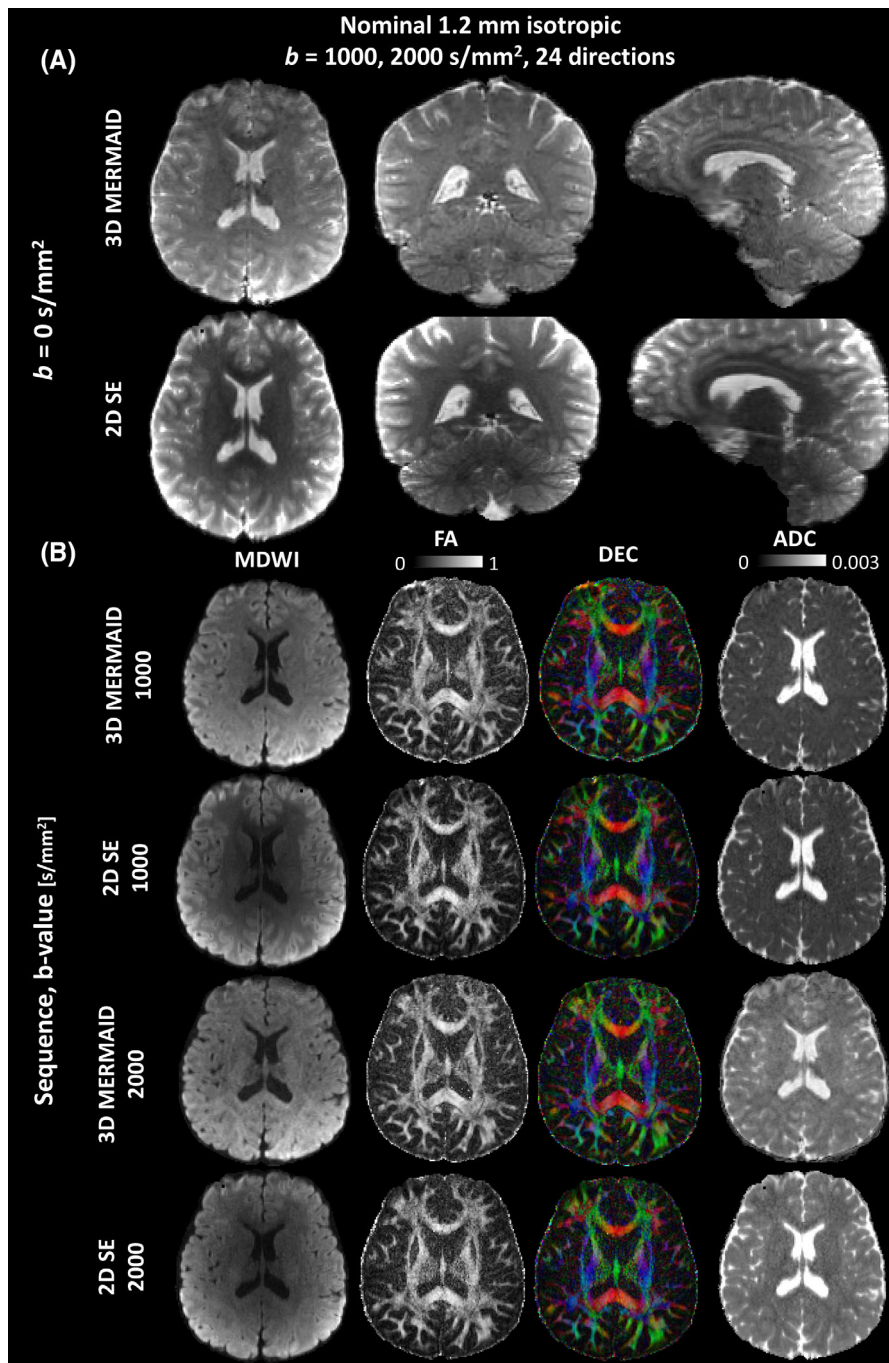


FIGURE 7 Comparison between diffusion measures calculated from a 2D SE and 3D MERMAID sequence with a matching scan time. (A) Shows different contrast between tissues in scans with no diffusion weighting. (B) Shows calculated diffusion parameters from 12 diffusion directions using the 3D MERMAID sequence compared to a standard 2D SE sequence. DEC, direction encoded color; FA, fractional anisotropy; MDWI, mean diffusion-weighted images.

Figure 9. The diffusion maps in the first row show small anatomical features such as blood vessels that are not visible at lower resolutions. Additional views of this data can be found in Figures S12–S17.

Zoomed-in areas of the fODFs overlaid on the anatomical scan show intricate details of various regions within the GM and WM. In Figure 9A, subcortical U-fibers connecting intracortical areas in the anteroposterior direction are visible. In Figure 9B, orientations of tangential and radial intracortical fibers in different layers as well as the projections of the WM into the cortex are displayed. The complex structure of crossing fibers in the WM is also shown in

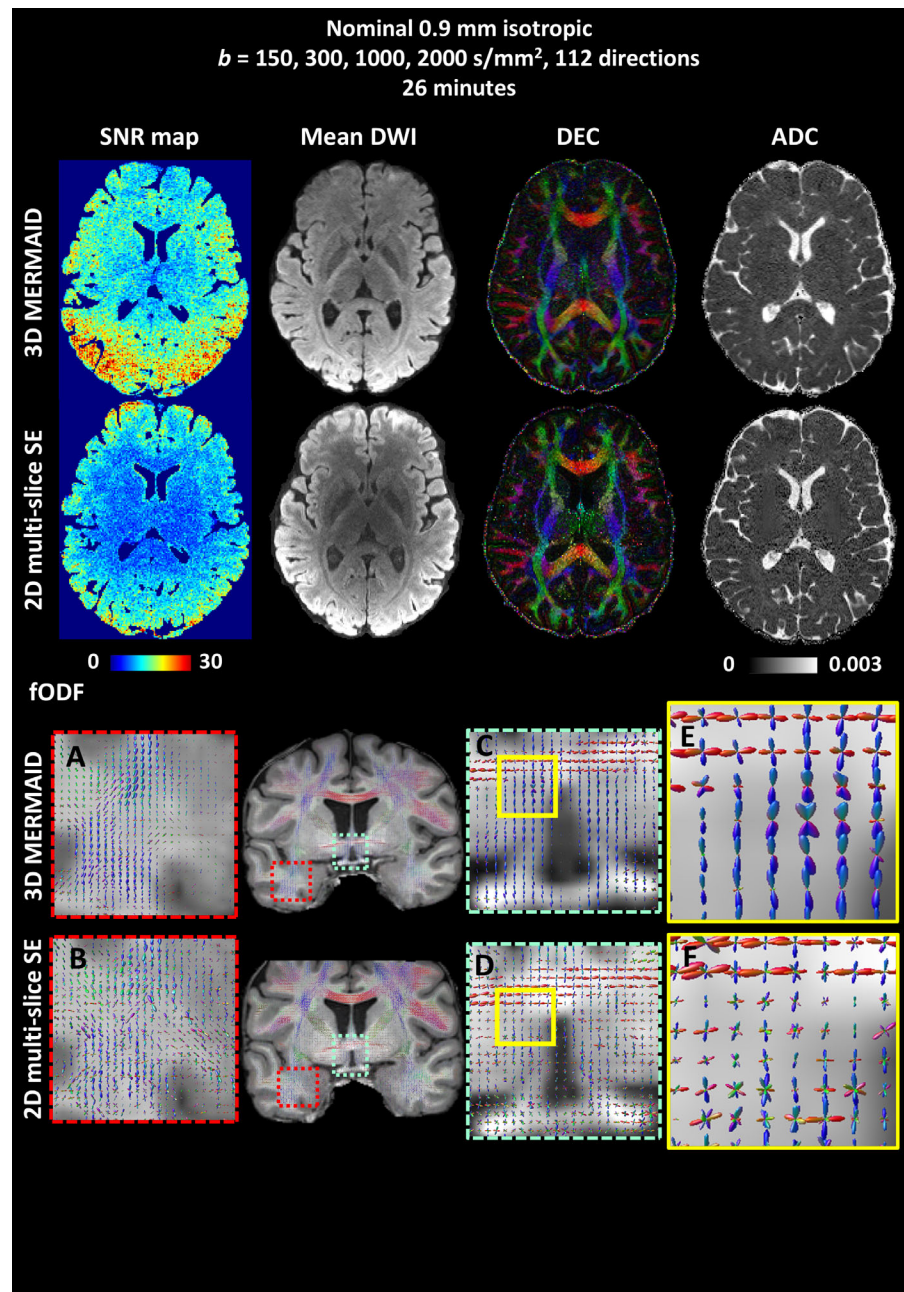
Figure 9C, and the small curvature of the hippocampus is detectable in Figure 9D.

4 | DISCUSSION

4.1 | SNR advantage of 3D MERMAID sequence over other 2D and 3D sequences

The comparison of multi-slice 2D SE and 3D MERMAID sequences in Figures 4, 7, and 8 show that SNR is enhanced for 3D MERMAID without increasing the scan

FIGURE 8 Comparison between high spatial- and angular-resolution scans of the 2D SE and 3D MERMAID sequences: SNR, MDWI, DEC, and ADC maps are shown in the top two rows. fODFs overlaid on the anatomical scan, and their zoomed-in images are shown below. Yellow boxes show enlarged areas of the zoomed-in images. fODFs, fiber orientation distribution functions.



time. This improvement can be used to increase the resolution of current multi-shell, high b -value, and advanced diffusion-encoding protocols. Additionally, the increased SNR per unit time can be leveraged to reduce the scan time of comparable resolutions and diffusion protocols currently achievable by 2D SE sequences by further accelerating the 3D MERMAID sequence. This will enable the acquisition of a higher number of diffusion directions in a shorter scan time.

As depicted in Figure 3C, the available signal, and therefore the SNR, increases almost exponentially as a function of TR. This presents a significant advantage compared to 2D SE and other 3D multi-slab sequences,

where SNR is increased by averaging as a function of $\sqrt{N_{\text{averages}}}$. The 3D MERMAID sequence is considerably more efficient for scans where longer acquisition times are permissible, as demonstrated in the 0.74 mm isotropic scan.

The RF pulse sequence design of the 3D MERMAID sequence enhances the SNR, as demonstrated in the phantom scans in Figure 4 that were reconstructed using SENSE. By incorporating CS into the image reconstruction pipeline, the apparent SNR is enhanced, as discussed extensively in Refs.17,84,85 This combined approach also allows for higher radial acceleration factors, resulting in greater SNR per unit time.

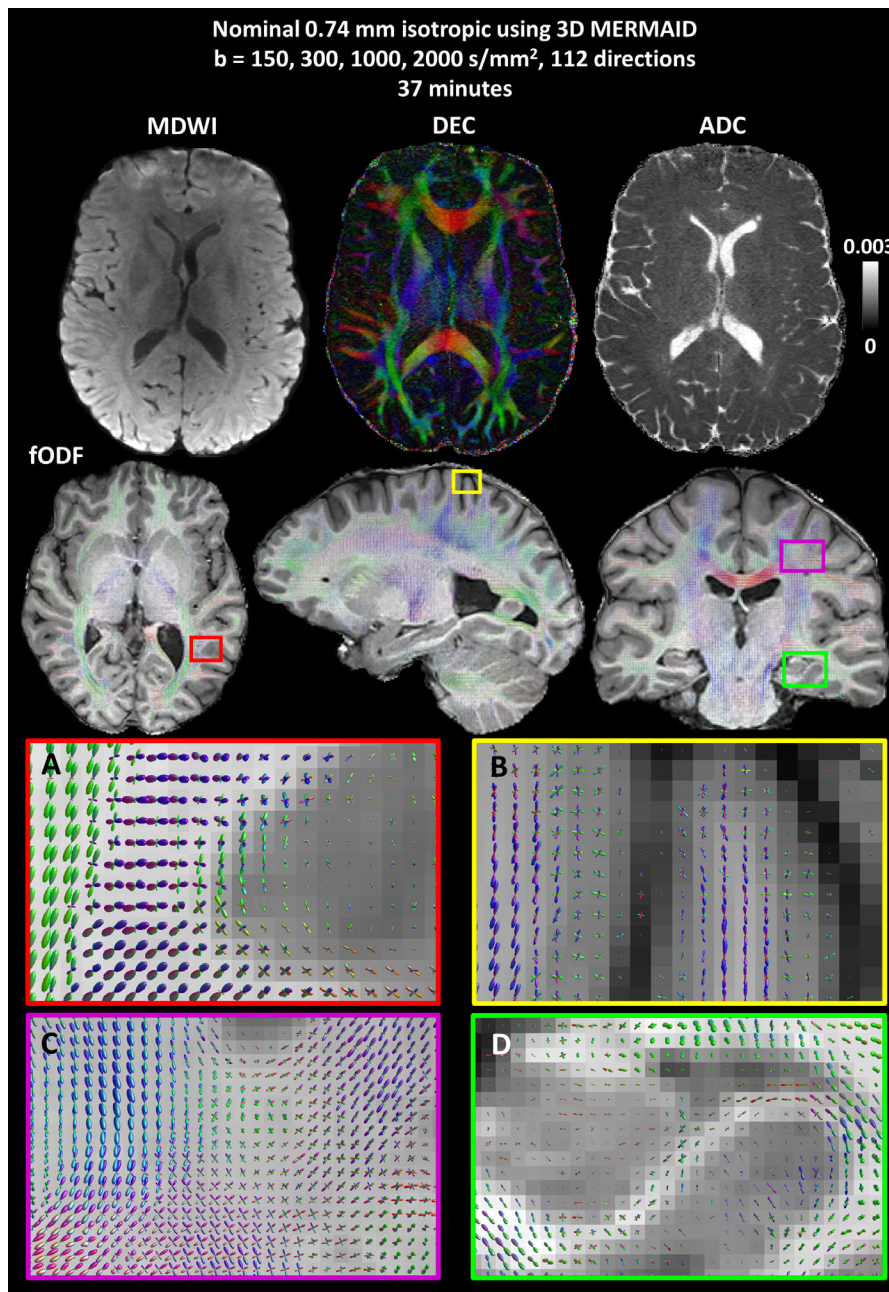


FIGURE 9 High-resolution diffusion maps and fODFs calculated from the nominal 0.74 mm isotropic scan, acquired using the 3D MERMAID sequence- diffusion maps in the first row, and fODFs overlaid on the MPRAGE scan in different orientations are shown in the second row. Zoomed-in areas, delineated by different box colors, reveal exquisite details of the intracortical fibers, WM crossing fibers, and the curvature of the hippocampus.

4.2 | Effective resolution of 3D MERMAID

We previously demonstrated in Ref. 86 that T_2^* decay causes blurring and lowers the effective image resolution, depending on the type of readout. In an EPI trajectory, the PE direction has the lowest bandwidth. Because the PE directions of the 2D EPI trajectory and TURBINE are the same, the resulting effective resolution in the PE direction is similar. For nominal resolutions of 1.5, 0.9, and 0.74 mm used, the effective resolutions are expected to be ~ 1.7 , ~ 1.2 , and ~ 0.93 mm,

respectively, which are $\sim 30\%$ lower than the nominal values.

In the 2D SE case, the resolution along the slice direction depends on the quality of the slice profile, whereas in the 3D MERMAID sequence, effects of CS reconstruction resulting from radial acceleration factors and the regularization parameter chosen, as well as the semi-Hanning filter, can slightly lower the effective resolution within the coronal plane, as seen in the coronal and sagittal views of Figures S3–S8. This can be compensated for by oversampling $\sim 20\%$ of the FE direction without a TE and readout time penalty.

4.3 | Microstructure modeling using 3D MERMAID

The 3D MERMAID sequence provides a novel contrast that includes both T_1 and T_2 weighting. According to Equations (1) and (2), both longitudinal and transverse magnetizations at steady state are sensitive to TE. Tissue relaxation rates are not considered in several diffusion-based microstructure models that compute compartmental volume fractions,²⁰ which in reality are T_2 -weighted signal fractions. To estimate true volume fractions, a co-encoded diffusion-relaxometry acquisition is required.^{87,88} Although the scans included in this work are suitable for microstructure modeling, the effect of the enhanced T_1 weighting on the compartmental signal fractions should be studied further in future work.

4.4 | Limitations

The short scan time of 3D MERMAID and phase-correction approach developed was achieved by using a single-shot EPI acquisition for each projection. However, this approach is limiting for very high spatial resolutions in which B_0 nonuniformities and higher eddy currents cause significant artifacts due to long readout times. For instance, the readout length for the scan with an isotropic resolution of 0.74 mm was 112.56 ms for $R_{\text{inplane}} = 3$, which causes significant B_0 nonuniformity artifacts and excessive T_2^* blurring. Reducing echo spacing shortens the readout time but also increases eddy current-induced artifacts due to higher gradient magnitudes. Techniques such as dual polarity GRAPPA,⁸⁹ better reference scans,^{90,91} and using a field monitoring system^{86,92–94} can help mitigate these artifacts, with an additional scan and/or image reconstruction time. These artifacts can also be minimized by segmenting the acquisition of each projection^{29,30} using EPTI^{38,95} or PSF.^{96,97} All three approaches increase scan time.

The SAR is relatively high for the 3D MERMAID sequence due to the additional inversion pulse and the use of adiabatic inversion and refocusing pulses, which may limit the TR for scans with a short readout train. Extending the duration of the adiabatic pulses can significantly reduce SAR without considerable loss of performance or increase in TE, for example, doubling the pulse duration of the inversion and refocusing results in a 40% reduction in SAR from ~80% to ~40%, and 3 ms increase in TE.

Imaging at ultrahigh fields will enhance the SNR per unit time of the 3D MERMAID.⁸⁶ However, the higher B_1^+ nonuniformity and increased SAR at ultrahigh field are two limiting factors for the 3D MERMAID sequence

due to its high sensitivity to B_1^+ nonuniformity and added inversion pulse. Parallel transmit approaches^{98–102} are needed to solve these limitations and achieve uniform high-resolution diffusion images at 7 T.

Removing corrupted projections prior to 3D image reconstruction increases the signal in the reconstructed image, as demonstrated in Figure 6B. However, in cases in which projections are neither corrupted nor removed, SNR decreases by an amount similar to that produced by a higher acceleration factor, calculated as $1/\sqrt{R}$, which corresponds to approximately an 11% reduction for removing 20% of the projections. The CS method used partially compensates for this SNR loss as discussed above, and reduces streaking artifacts associated with high acceleration factors.

Large-scale motion between shots will introduce artifacts in the final reconstructed images and causes variability in diffusion encoding across different shots. Compared to other multi-shot techniques, which involve significantly longer intervals between shots, the 3D MERMAID sequence is less affected due to its short effective TR per volume. In this study, we assumed this type of motion to be negligible during the effective TR of each volume, consistent with the assumption used in 2D SE sequences. Motion effects could be mitigated by using navigators acquired at short intervals, reconstructed from reordering the acquisition angle of projections to follow a Fibonacci sequence, as suggested in Graedel et al.⁶¹

Lastly, comparing the SNR plots of the phantom and human scans in Figures 4 and 8 shows that the SNR gain of 3D MERMAID compared to 2D SE for the human scan was lower than for the phantom scan, decreasing from ~50% to ~30%. This was expected due to the remaining small discrepancies between different projection magnitude images caused by the cardiac cycle. Using a cardiac-gated approach or motion-compensated gradients^{50,51,103} can potentially improve the SNR, but the trade-off between the SNR gain and longer TE and/or scan times should be considered.

5 | CONCLUSION

The 3D MERMAID sequence offers several advantages over typically used 2D and 3D acquisitions: higher SNR per unit time, shorter TR per volume compared to 2D multi-slice acquisitions, no slice/slab profile artifacts, better spin history, and better B_1^+ uniformity. These benefits become more pronounced in high- and ultrahigh-resolution imaging. The 3D MERMAID sequence balances the tradeoff between high-resolution k-space and q-space sampling. Preliminary results at 0.74 mm isotropic show the potential of this technique to

study small and complex structures in vivo in a reasonable scan time on clinical scanners.

ACKNOWLEDGMENTS

The authors would like to thank David Costa, Ronaldo Lopez, and Soheil Mollamohseni Quchani, the MRI technicians at the McConnell Brain Imaging Center, for their assistance with the human scans, Marcus Couch (Siemens Collaboration Scientist) for his technical support, Ilana Leppert for her technical suggestions and discussions on dMRI, Michael Ferreira for his help to make the phantom, Jennifer Campbell for her insights on microstructure modeling, Wen Da Lu for his suggestions and discussions on image registration, Mark Nelson for providing advanced normalization tools code for image registration, and all the volunteers who participated in the human scans.



FUNDING INFORMATION

This project was funded by the Natural Sciences and Engineering Research Council of Canada (NSERC-RGPIN-2018-05176), the Fonds de recherche du Québec-Santé (FRQS - CB-350681), Healthy Brains for Healthy Lives (HBHL), and the Killam Trusts. The data was acquired at the McConnell Brain Imaging Centre (The BIC), which is supported by the Canadian Foundation for Innovation (CFI), Brain Canada, and Healthy Brains for Health Lives.

DATA AVAILABILITY STATEMENT

The MatLab (MathWorks, Natick, MA) script (version 2021b) used for Bloch simulations and the image reconstruction pipelines described in Figures 2 and S2 are available at <https://github.com/TardifLab/3D-MERMAID>. Postprocessed diffusion data is available at <https://doi.org/10.5683/SP3/ULKLNy>.

ORCID

Sajjad Feizollah  <https://orcid.org/0000-0002-4340-1651>
Christine L. Tardif  <https://orcid.org/0000-0001-8356-6808>

REFERENCES

- Seehaus A, Roebroek A, Bastiani M, et al. Histological validation of high-resolution DTI in human post mortem tissue. *Front Neuroanat.* 2015;9:9.
- Seehaus AK, Roebroek A, Chiray O, et al. Histological validation of DW-MRI tractography in human postmortem tissue. *Cereb Cortex.* 2013;23:442-450.
- Roebroek A, Miller KL, Aggarwal M. Ex vivo diffusion MRI of the human brain: technical challenges and recent advances. *NMR Biomed.* 2019;32:e3941.
- Budde MD, Annesse J. Quantification of anisotropy and fiber orientation in human brain histological sections. *Front Integr Neurosci.* 2013;7:3.
- Leuze CWU, Anwender A, Bazin PL, et al. Layer-specific Intracortical connectivity revealed with diffusion MRI. *Cereb Cortex.* 2014;24:328-339.
- Aggarwal M, Nauen DW, Troncoso JC, Mori S. Probing region-specific microstructure of human cortical areas using high angular and spatial resolution diffusion MRI. *Neuroimage.* 2015;105:198-207.
- Ly M, Foley L, Manivannan A, Hitchens TK, Richardson RM, Modo M. Mesoscale diffusion magnetic resonance imaging of the ex vivo human hippocampus. *Hum Brain Mapp.* 2020;41:4200-4218.
- Zhao Z, Zhang L, Luo W, et al. Layer-specific microstructural patterns of anterior hippocampus in Alzheimer's disease with ex vivo diffusion MRI at 14.1 T. *Hum Brain Mapp.* 2023;44:458-471.
- Ke J, Foley LM, Hitchens TK, Richardson RM, Modo M. Ex vivo mesoscopic diffusion MRI correlates with seizure frequency in patients with uncontrolled mesial temporal lobe epilepsy. *Hum Brain Mapp.* 2020;41:4529-4548.
- Coras R, Milesi G, Zucca I, et al. 7T MRI features in control human hippocampus and hippocampal sclerosis: an ex vivo study with histologic correlations. *Epilepsia.* 2014;55:2003-2016.
- Knossalla F, Kohl Z, Winkler J, et al. High-resolution diffusion tensor-imaging indicates asymmetric microstructural disorganization within substantia nigra in early Parkinson's disease. *J Clin Neurosci.* 2018;50:199-202.
- Cardenas AM, Sarlls JE, Kwan JY, et al. Pathology of callosal damage in ALS: an ex-vivo, 7 T diffusion tensor MRI study. *Neuroimage Clin.* 2017;15:200-208.
- Noll DC, Nishimura DG, Macovski A. Homodyne detection in magnetic resonance imaging. *IEEE Trans Med Imaging.* 1991;10:154-163.
- Koopmans PJ, Pfaffenrot V. Enhanced POCS reconstruction for partial Fourier imaging in multi-echo and time-series acquisitions. *Magn Reson Med.* 2021;85:140-151.
- Griswold MA, Jakob PM, Heidemann RM, et al. Generalized autocalibrating partially parallel acquisitions (GRAPPA). *Magn Reson Med.* 2002;47:1202-1210.
- Pruessmann KP, Weiger M, Scheidegger MB, Boesiger P. SENSE: sensitivity encoding for fast MRI. *Magn Reson Med.* 1999;42:952-962.
- Lustig M, Donoho D, Pauly JM. Sparse MRI: the application of compressed sensing for rapid MR imaging. *Magn Reson Med.* 2007;58:1182-1195.
- Setsompop K, Gagoski BA, Polimeni JR, Witzel T, Wedeen VJ, Wald LL. Blipped-controlled aliasing in parallel imaging for simultaneous multislice echo planar imaging with reduced g-factor penalty. *Magn Reson Med.* 2012;67:1210-1224.
- Engel M, Mueller L, Döring A, Afzali M, Jones DK. Maximizing SNR per unit time in diffusion MRI with multiband T-hex spirals. *Magn Reson Med.* 2024;91:1323-1336.
- Zhang H, Schneider T, Wheeler-Kingshott CA, Alexander DC. NODDI: practical in vivo neurite orientation dispersion and density imaging of the human brain. *Neuroimage.* 2012;61:1000-1016.
- Jelescu IO, Veraart J, Fieremans E, Novikov DS. Degeneracy in model parameter estimation for multi-compartmental diffusion in neuronal tissue. *NMR Biomed.* 2016;29:33-47.

22. Novikov DS, Fieremans E, Jespersen SN, Kiselev VG. Quantifying brain microstructure with diffusion MRI: theory and parameter estimation. *NMR Biomed.* 2019;32:e3998.
23. Butts K, de Crespigny A, Pauly JM, Moseley M. Diffusion-weighted interleaved echo-planar imaging with a pair of orthogonal navigator echoes. *Magn Reson Med.* 1996;35:763-770.
24. Bammer R, Stollberger R, Augustin M, et al. Diffusion-weighted imaging with navigated interleaved echo-planar imaging and a conventional gradient system. *Radiology.* 1999;211:799-806.
25. Holdsworth SJ, Skare S, Newbould RD, Guzman R, Blevins NH, Bammer R. Readout-segmented EPI for rapid high resolution diffusion imaging at 3T. *Eur J Radiol.* 2008;65:36-46.
26. Porter DA, Heidemann RM. High resolution diffusion-weighted imaging using readout-segmented echo-planar imaging, parallel imaging and a two-dimensional navigator-based reacquisition. *Magn Reson Med.* 2009;62:468-475.
27. Liu C, Bammer R, Kim DH, Moseley ME. Self-navigated interleaved spiral (SNAILS): application to high-resolution diffusion tensor imaging. *Magn Reson Med.* 2004;52:1388-1396.
28. Tang X, Gao J, Aburas A, et al. Accelerated multi-b-value multi-shot diffusion-weighted imaging based on EPI with keyhole and a low-rank tensor constraint. *Magn Reson Imaging.* 2024;110:138-148.
29. Chen NK, Guidon A, Chang HC, Song AW. A robust multi-shot scan strategy for high-resolution diffusion weighted MRI enabled by multiplexed sensitivity-encoding (MUSE). *Neuroimage.* 2013;72:41-47.
30. Guhaniyogi S, Chu ML, Chang HC, Song AW, Chen N. Motion immune diffusion imaging using augmented MUSE for high-resolution multi-shot EPI. *Magn Reson Med.* 2016;75:639-652.
31. Mani M, Jacob M, Kelley D, Magnotta V. Multi-shot sensitivity-encoded diffusion data recovery using structured low-rank matrix completion (MUSSELS). *Magn Reson Med.* 2017;78:494-507.
32. Li Z, Miller KL, Chen X, Chiew M, Wu W. Self-navigated 3D diffusion MRI using an optimized CAIPI sampling and structured low-rank reconstruction estimated navigator. *IEEE transactions on medical imaging.* 2024 Sep 6:1.
33. Pipe JG. Motion correction with PROPELLER MRI: application to head motion and free-breathing cardiac imaging. *Magn Reson Med.* 1999;42:963-969.
34. Pipe JG, Zwart N. Turboprop: improved PROPELLER imaging. *Magn Reson Med.* 2006;55:380-385.
35. Li Z, Pipe JG, Lee CY, Debbins JP, Karis JP, Huo D. X-PROP: a fast and robust diffusion-weighted propeller technique. *Magn Reson Med.* 2011;66:341-347.
36. Scherrer B, Gholipour A, Warfield SK. Super-resolution in diffusion-weighted imaging. *Med Image Comput Comput Assist Interv.* 2011;14:124-132.
37. Vis G, Nilsson M, Westin CF, Szczepankiewicz F. Accuracy and precision in super-resolution MRI: enabling spherical tensor diffusion encoding at ultra-high b-values and high resolution. *Neuroimage.* 2021;245:118673.
38. Dong Z, Reese TG, Lee HH, et al. Romer-EPTI: rotating-view motion-robust super-resolution EPTI for SNR-efficient distortion-free in-vivo mesoscale diffusion MRI and microstructure imaging. *Magn Reson Med.* 2025;93:1535-1555.
39. Bruce IP, Chang HC, Petty C, Chen NK, Song AW. 3D-MB-MUSE: a robust 3D multi-slab, multi-band and multi-shot reconstruction approach for ultrahigh resolution diffusion MRI. *Neuroimage.* 2017;159:46-56.
40. Engström M, Skare S. Diffusion-weighted 3D multislabs echo planar imaging for high signal-to-noise ratio efficiency and isotropic image resolution. *Magn Reson Med.* 2013;70:1507-1514.
41. Frost R, Miller KL, Tijssen RHN, Porter DA, Jezzard P. 3D multi-slab diffusion-weighted readout-segmented EPI with real-time cardiac-reordered k-space acquisition. *Magn Reson Med.* 2014;72:1565-1579.
42. Setsompop K, Fan Q, Stockmann J, et al. High-resolution in vivo diffusion imaging of the human brain with generalized slice dithered enhanced resolution: simultaneous multislice (gSlider-SMS). *Magn Reson Med.* 2018;79:141-151.
43. Wang F, Bilgic B, Dong Z, et al. Motion-robust sub-millimeter isotropic diffusion imaging through motion corrected generalized slice dithered enhanced resolution (MC-gSlider) acquisition. *Magn Reson Med.* 2018;80:1891-1906.
44. Ramos-Llordén G, Ning L, Liao C, et al. High-fidelity, accelerated whole-brain submillimeter in vivo diffusion MRI using gSlider-spherical ridgelets (gSlider-SR). *Magn Reson Med.* 2020;84:1781-1795.
45. Liao C, Bilgic B, Tian Q, et al. Distortion-free, high-isotropic-resolution diffusion MRI with gSlider BUDA-EPI and multicoil dynamic B_0 shimming. *Magn Reson Med.* 2021;86:791-803.
46. Zhang Q, Coolen BF, Nederveen AJ, Strijkers GJ. Three-dimensional diffusion imaging with spiral encoded navigators from stimulated echoes (3D-DISPENSE). *Magn Reson Med.* 2019;81:1052-1065.
47. Jeong EK, Kim SE, Parker DL. High-resolution diffusion-weighted 3D MRI, using diffusion-weighted driven-equilibrium (DW-DE) and multishot segmented 3D-SSFP without navigator echoes. *Magn Reson Med.* 2003;50:821-829.
48. McNab JA, Gallichan D, Miller KL. 3D steady-state diffusion-weighted imaging with trajectory using radially batched internal navigator echoes (TURBINE). *Magn Reson Med.* 2010;63:235-242.
49. Li H, Zu T, Chen R, et al. 3D diffusion MRI with twin navigator-based GRASE and comparison with 2D EPI for tractography in the human brain. *Magn Reson Med.* 2023;90:1969-1978.
50. Stoeck CT, von Deuster C, Genet M, Atkinson D, Kozerke S. Second-order motion-compensated spin echo diffusion tensor imaging of the human heart. *Magn Reson Med.* 2016;75:1669-1676.
51. Szczepankiewicz F, Sjölund J, Dall'Armellina E, et al. Motion-compensated gradient waveforms for tensor-valued diffusion encoding by constrained numerical optimization. *Magn Reson Med.* 2021;85:2117-2126.
52. Michael ES, Hennel F, Pruessmann KP. Motion-compensated diffusion encoding in multi-shot human brain acquisitions: insights using high-performance gradients. *Magn Reson Med.* 2024;92:556-572.
53. Jelescu IO, de Skowronski A, Geffroy F, Palombo M, Novikov DS. Neurite exchange imaging (NEXI): a minimal model of

- diffusion in gray matter with inter-compartment water exchange. *Neuroimage*. 2022;256:119277.
54. Uhl Q, Pavan T, Molendowska M, Jones DK, Palombo M, Jelescu IO. Quantifying human gray matter microstructure using neurite exchange imaging (NEXI) and 300 mT/m gradients. *Imaging Neurosci*. 2024;2:1-19.
 55. Palombo M, Ianus A, Guerrieri M, et al. SANDI: a compartment-based model for non-invasive apparent soma and neurite imaging by diffusion MRI. *Neuroimage*. 2020;215:116835.
 56. Feizollah S, Tardif C. Multi-shot 3D diffusion MRI sequence for a fast and high-resolution imaging at 3T. In Proceedings of the 32nd Annual Joint ISMRM & ISMRT Meeting, Singapore 2024.
 57. Cox EF, Gowland PA. Simultaneous quantification of T_2 and T_2^* using a combined gradient echo-spin echo sequence at ultrahigh field. *Magn Reson Med*. 2010;64:1440-1445.
 58. Rooney WD, Johnson G, Li X, et al. Magnetic field and tissue dependencies of human brain longitudinal $1H_2O$ relaxation in vivo. *Magn Reson Med*. 2007;57:308-318.
 59. Bloch F. Nuclear induction. *Phys Rev*. 1946;70:460-474.
 60. Ernst RR, Anderson WA. Application of Fourier transform spectroscopy to magnetic resonance. *Rev Sci Instrum*. 1966;37:93-102.
 61. Graedel NN, Miller KL, Chiew M. Ultrahigh resolution fMRI at 7T using radial-Cartesian TURBINE sampling. *Magn Reson Med*. 2022;88:2058-2073.
 62. Heid O. Method for the phase correction of nuclear magnetic resonance signals. 2000 <https://patents.google.com/patent/US6043651A/en>. Accessed March 17, 2024.
 63. Uecker M, Hohage T, Block KT, Frahm J. Image reconstruction by regularized nonlinear inversion—joint estimation of coil sensitivities and image content. *Magn Reson Med*. 2008;60:674-682. doi:10.1002/mrm.21691
 64. Skare S, Holdsworth S, Newbould RD, Bammer R. On the battle between Rician noise and phase-interferences in DWI. *Proceedings of the 17th Annual Meeting of ISMRM*. ISMRM; 2009:1409.
 65. Pipe JG, Farthing VG, Forbes KP. Multishot diffusion-weighted FSE using PROPELLER MRI. *Magn Reson Med*. 2002;47:42-52.
 66. Wang FN, Huang TY, Lin FH, et al. PROPELLER EPI: an MRI technique suitable for diffusion tensor imaging at high field strength with reduced geometric distortions. *Magn Reson Med*. 2005;54:1232-1240.
 67. Wang X, Rosenzweig S, Scholand N, Holme HCM, Uecker M. Data for: model-based reconstruction for simultaneous multi-slice T_1 mapping using single-shot inversion-recovery radial FLASH. *Magn Reson Med*. 2020;85:1258-1271.
 68. Uecker M, Lai P, Murphy MJ, et al. ESPIRiT—an eigenvalue approach to autocalibrating parallel MRI: where SENSE meets GRAPPA. *Magn Reson Med*. 2014;71:990-1001.
 69. Andersson JLR, Skare S, Ashburner J. How to correct susceptibility distortions in spin-echo echo-planar images: application to diffusion tensor imaging. *Neuroimage*. 2003;20:870-888.
 70. Smith SM, Jenkinson M, Woolrich MW, et al. Advances in functional and structural MR image analysis and implementation as FSL. *Neuroimage*. 2004;23:S208-S219.
 71. Tournier JD, Smith R, Raffelt D, et al. MRtrix3: a fast, flexible and open software framework for medical image processing and visualisation. *Neuroimage*. 2019;202:116137.
 72. Basser PJ, Mattiello J, LeBihan D. Estimation of the effective self-diffusion tensor from the NMR spin echo. *J Magn Reson B*. 1994;103:247-254.
 73. Veraart J, Sijbers J, Sunaert S, Leemans A, Jeurissen B. Weighted linear least squares estimation of diffusion MRI parameters: strengths, limitations, and pitfalls. *Neuroimage*. 2013;81:335-346.
 74. Mussard E, Hilbert T, Forman C, Meuli R, Thiran JP, Kober T. Accelerated MP2RAGE imaging using Cartesian phyllotaxis readout and compressed sensing reconstruction. *Magn Reson Med*. 2020;84:1881-1894.
 75. Moeller S, Pisharady PK, Ramanna S, et al. NOise reduction with DIstribution corrected (NORDIC) PCA in dMRI with complex-valued parameter-free locally low-rank processing. *Neuroimage*. 2021;226:117539.
 76. Dhollander T, Mito R, Raffelt D, Connelly A. Improved white matter response function estimation for 3-tissue constrained spherical deconvolution. In Proceedings of the 27th Annual Meeting of ISMRM, Montréal, Québec, Canada, 2019. p. 555.
 77. Jeurissen B, Tournier JD, Dhollander T, Connelly A, Sijbers J. Multi-tissue constrained spherical deconvolution for improved analysis of multi-shell diffusion MRI data. *Neuroimage*. 2014;103:411-426.
 78. Tournier JD, Calamante F, Gadian DG, Connelly A. Direct estimation of the fiber orientation density function from diffusion-weighted MRI data using spherical deconvolution. *Neuroimage*. 2004;23:1176-1185.
 79. Raffelt D, Dhollander T, Tournier JD, et al. Bias field correction and intensity normalisation for quantitative analysis of apparent fibre density. In Proceedings of the 25th Annual Meeting of ISMRM, Honolulu, HI, 2017. p. 3541.
 80. Dhollander T, Tabbara R, Rosnarho-Tornstrand J, Tournier JD, Raffelt D, Connelly A. Multi-tissue log-domain intensity and inhomogeneity normalisation for quantitative apparent fibre density. In Proceedings of the 29th Annual Meeting of ISMRM: An Online Experience, 2021. p. 2472.
 81. Avants BB, Tustison N, Song G. Advanced normalization tools (ANTS). *Insight J*. 2009;2:1-35.
 82. Tardif CL, Schäfer A, Waehnert M, Dinse J, Turner R, Bazin PL. Multi-contrast multi-scale surface registration for improved alignment of cortical areas. *Neuroimage*. 2015;111:107-122.
 83. Zhang Y, Brady M, Smith S. Segmentation of brain MR images through a hidden Markov random field model and the expectation-maximization algorithm. *IEEE Trans Med Imaging*. 2001;20:45-57.
 84. Haldar JP, Hernando D, Liang ZP. Compressed-sensing MRI with random encoding. *IEEE Trans Med Imaging*. 2011;30:893-903.
 85. Ye JC. Compressed sensing MRI: a review from signal processing perspective. *BMC Biomed Eng*. 2019;1:8.
 86. Feizollah S, Tardif CL. High-resolution diffusion-weighted imaging at 7 Tesla: single-shot readout trajectories and their impact on signal-to-noise ratio, spatial resolution and accuracy. *Neuroimage*. 2023;274:120159.
 87. Frigo M, Fick RHJ, Zucchelli M, Deslauriers-Gauthier S, Deriche R. Multi tissue modelling of diffusion MRI signal reveals volume fraction bias. 2020 *IEEE 17th International Symposium on Biomedical Imaging (ISBI)*. IEEE; 2020:991-994.

88. Veraart J, Novikov DS, Fieremans E. TE dependent diffusion imaging (TEDDI) distinguishes between compartmental T_2 relaxation times. *Neuroimage*. 2018;182:360-369.
89. Hoge WS, Polimeni JR. Dual-polarity GRAPPA for simultaneous reconstruction and ghost correction of EPI data. *Magn Reson Med*. 2016;76:32-44.
90. Talagala SL, Sarlls JE, Liu S, Inati SJ. Improvement of temporal signal-to-noise ratio of GRAPPA accelerated echo planar imaging using a FLASH based calibration scan. *Magn Reson Med*. 2016;75:2362-2371.
91. Polimeni JR, Bhat H, Witzel T, et al. Reducing sensitivity losses due to respiration and motion in accelerated echo planar imaging by reordering the autocalibration data acquisition. *Magn Reson Med*. 2016;75:665-679.
92. Veldmann M, Edwards LJ, Pine KJ, et al. Improving MR axon radius estimation in human white matter using spiral acquisition and field monitoring. *Magn Reson Med*. 2024;92:1898-1912.
93. Lee Y, Wilm BJ, Brunner DO, et al. On the signal-to-noise ratio benefit of spiral acquisition in diffusion MRI. *Magn Reson Med*. 2021;85:1924-1937.
94. Ma R, Akçakaya M, Moeller S, Auerbach E, Uğurbil K, Van de Moortele PF. A field-monitoring-based approach for correcting eddy-current-induced artifacts of up to the 2nd spatial order in human-connectome-project-style multiband diffusion MRI experiment at 7T: a pilot study. *Neuroimage*. 2020;216:116861.
95. Fair MJ, Liao C, Manhard MK, Setsompop K. Diffusion-PEPTIDE: distortion- and blurring-free diffusion imaging with self-navigated motion-correction and relaxometry capabilities. *Magn Reson Med*. 2021;85:2417-2433.
96. In MH, Posnansky O, Speck O. High-resolution distortion-free diffusion imaging using hybrid spin-warp and echo-planar PSF-encoding approach. *Neuroimage*. 2017;148:20-30.
97. Dong Z, Wang F, Reese TG, et al. Tilted-CAIPI for highly accelerated distortion-free EPI with point spread function (PSF) encoding. *Magn Reson Med*. 2019;81:377-392.
98. Gras V, Vignaud A, Amadon A, Le Bihan D, Boulant N. Universal pulses: a new concept for calibration-free parallel transmission. *Magn Reson Med*. 2017;77:635-643.
99. Khaneja N, Reiss T, Kehlet C, Schulte-Herbrüggen T, Glaser SJ. Optimal control of coupled spin dynamics: design of NMR pulse sequences by gradient ascent algorithms. *J Magn Reson*. 2005;172:296-305.
100. Gras V, Mauconduit F, Vignaud A, et al. Design of universal parallel-transmit refocusing kT-point pulses and application to 3D T_2 -weighted imaging at 7T. *Magn Reson Med*. 2018;80:53-65.
101. Lowen D, Pracht ED, Gras V, et al. Design of calibration-free RF pulses for T-weighted single-slab 3D turbo-spin-echo sequences at 7T utilizing parallel transmission. *Magn Reson Med*. 2024;92:2037-2050.
102. Feizollah S, Lowen D, Couch M, Pracht ED, Stöcker T, Tardif C. 3D diffusion MRI at 7T with universal pulses for improved image uniformity. In Proceedings of the 32nd Annual Joint ISMRM & ISMRT Meeting, Singapore, 2024.
103. Nguyen C, Fan Z, Sharif B, et al. In vivo three-dimensional high resolution cardiac diffusion-weighted MRI: a motion compensated diffusion-prepared balanced steady-state free precession approach. *Magn Reson Med*. 2014;72:1257-1267.

SUPPORTING INFORMATION

Additional supporting information may be found in the online version of the article at the publisher's website.

Figure S1. Output of each image reconstruction step described in section 2.2. (A, B) are triangle and semi-Hanning filters, respectively.

Figure S2. 3D multi-shot enhanced recovery motion insensitive diffusion (MERMAID) image reconstruction pipeline including denoising. First all projections of all volumes are reconstructed, then denoising (NORDIC) is performed for each coil channel individually. In the next step, denoised projections are used to reconstruct every volume as in the pipeline described in Figure 2 of the paper.

Figure S3. Signal-to-noise ratio (SNR) maps of 3D multi-shot enhanced recovery motion insensitive diffusion (MERMAID) and 2D SE at nominal resolution of 0.9.

Figure S4. Diffusion images of $b = 1000 \text{ s/mm}^2$ with nominal isotropic resolution of 0.9 mm.

Figure S5. Diffusion images of $b = 2000 \text{ s/mm}^2$ with nominal isotropic resolution of 0.9 mm.

Figure S6. Mean diffusion-weighted images (MDWI) of 3D multi-shot enhanced recovery motion insensitive diffusion (MERMAID) and 2D SE at nominal resolution of 0.9.

Figure S7. Direction encoded color (DEC) maps of 3D multi-shot enhanced recovery motion insensitive diffusion (MERMAID) and 2D SE at nominal resolution of 0.9.

Figure S8. Apparent diffusion coefficient (ADC) maps of 3D multi-shot enhanced recovery motion insensitive diffusion (MERMAID) and 2D SE at nominal resolution of 0.9.

Figure S9. Axial fiber orientation distribution functions (fODFs) of 3D multi-shot enhanced recovery motion insensitive diffusion (MERMAID) and 2D SE overlaid on the MPRAGE scan.

Figure S10. coronal fiber orientation distribution functions (fODFs) of 3D multi-shot enhanced recovery motion insensitive diffusion (MERMAID) and 2D SE overlaid on the MPRAGE scan.

Figure S11. Sagittal fiber orientation distribution functions (fODFs) of 3D multi-shot enhanced recovery motion insensitive diffusion (MERMAID) and 2D SE overlaid on the MPRAGE scan.

Figure 12. Diffusion images of $b = 1000 \text{ s/mm}^2$ with nominal isotropic resolution of 0.74 mm.

Figure 13. Diffusion images of $b = 2000 \text{ s/mm}^2$ with nominal isotropic resolution of 0.74 mm.

Figure S14. Mean diffusion-weighted images (MDWI) of nominal isotropic 0.74 scan.

Figure S15. Direction encoded color (DEC) maps of nominal isotropic 0.74 mm scan.

Figure S16. Apparent diffusion coefficient (ADC) map of nominal isotropic 0.74 mm scan.

Figure S17. Fractional anisotropy (FA) map of nominal isotropic 0.74 mm scan.

Movie S1. Magnitude (left) and phase (right) images of reconstructed projections for $b = 0 \text{ s/mm}^2$ before phase correction- slight changes due to the cardiac cycle appear in magnitude and phase images.

Movie S2. Magnitude (left) and phase (right) images of reconstructed projections for $b = 1000 \text{ s/mm}^2$ before phase

correction- the diffusion contrast causes significant phase differences between shots. A slight signal drop in magnitude images is also visible.

Movie S3. Magnitude (left) and phase (right) images of reconstructed projections for $b = 2000 \text{ s/mm}^2$ before phase correction- considerable phase differences between shots are visible, as well as signal drop due to the cardiac cycle.

How to cite this article: Feizollah S, Tardif CL. 3D MERMAID: 3D Multi-shot enhanced recovery motion artifact insensitive diffusion for submillimeter, multi-shell, and SNR-efficient diffusion imaging. *Magn Reson Med*. 2025;93:2311-2330. doi: 10.1002/mrm.30436